

RESEARCH ARTICLE | AUGUST 07 2023

Study of backward Brillouin scattering in gas-filled anti-resonant fibers

Malak Galal ; Li Zhang ; Shoufei Gao; Yingying Wang; Luc Thévenaz 



APL Photonics 8, 086104 (2023)


<https://doi.org/10.1063/5.0151018>



Export
Citation

CrossMark

07 August 2023 19:29:08



THE ADVANCED MATERIALS MANUFACTURER®

yttrium iron garnet glassy carbon beamsplitters fused quartz additive manufacturing

zeolites III-IV semiconductors gallium lump copper nanoparticles organometallics

nano ribbons barium fluoride europium phosphors photonics infrared dyes

sapphire windows Nd:YAG epitaxial crystal growth ultra high purity materials transparent ceramics CIGS

spintronics raman substrates cerium oxide polishing powder cermet nanodispersions

silver nanoparticles perovskites surface functionalized nanoparticles MBE grade materials thin film

MOCVD beta-barium borate Os Ir Pt Au Ag Cu Zn Ga Ge As Se Br Kr

rare earth metals quantum dots Os Ir Pt Au Ag Cu Zn Ga Ge As Se Br Kr

osmium scintillation Ce:YAG Os Ir Pt Au Ag Cu Zn Ga Ge As Se Br Kr

refractory metals laser crystals Os Ir Pt Au Ag Cu Zn Ga Ge As Se Br Kr

anodic aluminum oxide niobate InAs wafers MOFs AuNPs ZnS CdTe perovskite crystals transparent ceramics

YBCO superconductors InGaAs indium tin oxide MgF₂ rutile optical glass

metamaterials borosilicate glass diamond micropowder

Now Invent.™

www.americanelements.com

© 2001-2023, American Elements LLC, a U.S. Registered Trademark

The Next Generation of Material Science Catalogs

Study of backward Brillouin scattering in gas-filled anti-resonant fibers

Cite as: APL Photon. 8, 086104 (2023); doi: 10.1063/5.0151018

Submitted: 17 March 2023 • Accepted: 28 June 2023 •

Published Online: 7 August 2023



Malak Galal,^{1,a)} Li Zhang,^{1,b)} Shoufei Gao,² Yingying Wang,² and Luc Thévenaz¹

AFFILIATIONS

¹ École Polytechnique Fédérale de Lausanne, SCI-STI-LT Station 11, 1015 Lausanne, Switzerland

² Institute of Photonics Technology, Jinan University, Guangzhou 510632, China

^{a)} Author to whom correspondence should be addressed: m.galal93@gmail.com

^{b)} Current Address: Istituto Italiano di Tecnologia, Viale Regina Elena 291, 00161 Rome, Italy.

ABSTRACT

Brillouin scattering in gas shows unmatched gain properties in hollow-core optical fibers filled at high pressure. Here, the gain characteristics are studied for two common gases, namely, N₂ and CO₂, which show distinct features and are compared to expected responses deduced from conventional thermodynamic models for gases. This is realized—for the first time to our knowledge—in anti-resonant hollow-core optical fibers, demonstrating their full suitability for generating and exploiting Brillouin amplification in fluidic media. The potential of Brillouin scattering in gases is manifested in a distributed temperature sensor that is totally immune to strain and benefits from the absence of shear stress in the gaseous medium. The experimental results presented indicate that gases with smaller molecular masses show a higher temperature sensitivity than gases with larger masses. This inverse proportionality between the temperature sensitivity and the molecular mass of a gas shown in the experiment qualitatively agrees with the ideal gas model.

© 2023 Author(s). All article content, except where otherwise noted, is licensed under a Creative Commons Attribution (CC BY) license (<http://creativecommons.org/licenses/by/4.0/>). <https://doi.org/10.1063/5.0151018>

I. INTRODUCTION

With the rise of the propitious emerging field of gas photonics comes the advent of a new era where a unique synergy is formed between gas, light, and glass. This three-element relationship has come to light as a consequence of the continuous development of novel optical fibers, particularly hollow-core optical fibers (HCFs), in the hope and quest of the scientific community to possibly break the silica loss floor.¹ In that regard, a vast amount of research oriented toward the fabrication of novel HCFs^{2–8} has successfully led to the demonstration of exceptionally-low propagation loss (0.174 dB/km) using hollow-core anti-resonant optical fibers.⁹ Such fibers are rapidly proving themselves as highly promising candidates given their ultra-low loss, optical nonlinearity, and chromatic dispersion over a broad bandwidth with near-vacuum latency.⁷

One interesting point worth noting is the fact that even though HCFs demonstrate a very low optical nonlinearity given their holey nature, they are also capable of providing a viable medium for light-matter interactions when filled with a suitable substance, as has been shown using hollow-core photonic-crystal fibers

(HC-PCFs).^{10,11} Additionally, due to their hollow cores, HCFs can provide long interaction lengths for wave coupling, and their threshold for high optical power damage is significantly larger than that of conventional silica fibers. The first demonstration measuring Raman scattering in hydrogen-filled HC-PCFs was presented in Ref. 10. In other recent studies,^{12,13} Brillouin scattering in high-pressure gas-filled HC-PCF and in the surroundings of a nano-fiber was demonstrated. In Ref. 12, the Brillouin gain was found to be proportional to the square of the gas pressure, and a 6× higher Brillouin gain over that observed in silica-core fibers was reported. Such results are particularly intriguing, as the medium of the light-matter interaction in this case (unlike in solid silica) is variable. This, in turn, means that the same hollow-core fiber can be filled with different gases, gas mixtures, or other fluids, and their behaviors can be compared under the same exact experimental conditions.

Utilizing Brillouin scattering for such experiments is currently an emerging approach in several types of applications such as in the microscopy field,^{14,15} as it has the capabilities to enhance our understanding of important physical parameters of substances as

well as their viscoelastic properties, which usually require sophisticated techniques to unravel. Additionally, spectroscopy in gas-filled hollow-core fibers used for gas sensing has been presented in several works in the literature.^{16,17} Particularly, the work presented in Ref. 16 showed photo-acoustic spectroscopy based on forward Brillouin scattering in acetylene-filled anti-resonant fibers and characterized inhomogeneities along the fiber. It is, therefore, of particular interest to further explore the use of gases and compare the behavior of different substances confined within the hollow cores of the fibers to understand more about the substances under these conditions and their potential for sensing applications. So far, all the reported works measuring backward Brillouin scattering utilizing this gas-filled HCF platform have not presented thorough analyses for the behaviors of different gases. Additionally, in their investigations, they always relied on HC-PCFs in the experiments, and none have considered using anti-resonant HCFs instead, despite the remarkable advantages the latter fibers offer.

Even though they have proven themselves to be good candidates for optical sensing and nonlinearity, HC-PCFs have never reached the expectation of offering extremely low back-scattering loss for optical communication, and this is because of the limiting frozen-in surface capillary waves that are excited by the thermal background.¹⁸ Anti-resonant fibers, on the other hand, have a smaller overlap of the optical field with the glass surfaces in comparison with photonic crystal fibers, which reduces surface scattering and makes it possible to reach very low propagation losses. Such fibers not only exhibit similar capabilities as those provided by HC-PCFs but also offer additional advantages, such as quasi-single mode propagation, that make them stand out as potential candidates for opening new avenues in the fields of optical nonlinearity, laser development, optical sensing, and many more.

Therefore, here, we investigate for the first time light–gas opto-acoustic interaction in gas-filled anti-resonant HCFs based on Brillouin reflectometry (i.e., requiring only a single fiber end). Brillouin scattering in anti-resonant HCFs is demonstrated using two different anti-resonant HCFs, which are the conjoined-tube anti-resonant fiber (HC-CAF) and the revolver anti-resonant fiber (HC-RAF), using two different gases, namely, nitrogen (N₂) and carbon dioxide (CO₂) gases, as they are among the most common gas species that are ubiquitous in various terrestrial environments. A rigorous investigation is performed to analyze the effect of the different gases in terms of opto-acoustic interaction while confined within the fibers. From the Brillouin gain spectra, we obtain the Brillouin properties given by the acoustic properties of the gas inside the fibers (sound velocity and acoustic loss). We also conducted an overall comparison between the two HC-ARFs and one HC-PCF. Furthermore, we perform a highly-sensitive distributed temperature measurement based on Brillouin optical correlation-domain reflectometry (BOCDR) using gas-filled anti-resonant HCFs. Based on our experimental results, we show that different gases exhibit significantly different sensitivities to temperature changes. The work presented here, pointing out the high Brillouin light amplification and the distributed Brillouin temperature sensing in anti-resonant HCFs for different gases, highlights the great potential of gas-filled anti-resonant HCFs as suitable platforms for lasing, filtering, amplifying, and sensing applications.

II. ESTIMATION OF THE BRILLOUIN GAIN

A. Brillouin frequency shift and gain

Brillouin scattering describes the light interaction with the slow collective oscillation of the molecular medium (acoustic phonons with low energy and high momentum), where there is mode-coupling and energy transfer between the optical and the vibrational modes of the entire medium.^{19,20} Spontaneous Brillouin scattering takes place when light is scattered by thermally-activated sound waves, resulting in frequency-shifted scattered waves (down-shifted Stokes scattering through phonon creation and up-shifted anti-Stokes scattering through phonon annihilation). Since Brillouin scattering involves coupling between optical waves and high-momentum propagating acoustic waves, the interaction requires the phase matching between the involved waves to be stringent. When the phase-matching condition is met, the frequency of the sound wave is given by the following expression:^{19,20}

$$\nu_B = 2n_{\text{eff}} \frac{\nu_a}{\lambda_0}, \quad (1)$$

showing that the Brillouin spectral shift ν_B of the scattered waves is directly proportional to the acoustic velocity ν_a , n_{eff} is the effective refractive index of the optical mode, and λ_0 is the wavelength of the incident light in vacuum. The efficiency in the coupling between the two waves is determined by the acousto-optic overlap effective area (A_{ao}), which is discussed in more detail in Sec. II C, and the Brillouin gain coefficient is inversely proportional to A_{ao} as follows:^{19,20}

$$g_B = \frac{\gamma_e^2 \omega^2}{n \nu_a c^3 \rho \Gamma_B A_{\text{ao}}}, \quad (2)$$

where $\gamma_e = \rho \frac{\partial \epsilon_r}{\partial \rho}$ is the electrostrictive coefficient in the medium and is described as the normalized rate of change of the relative permittivity ϵ_r with respect to the medium density ρ , ω is the angular frequency of the light, n is the medium refractive index, c is the speed of light in vacuum, ν_a is the longitudinal acoustic velocity, and Γ_B is the relevant acoustic attenuation.

B. Brillouin linewidth

The Brillouin linewidth [i.e., full width at half maximum (FWHM) of the Lorentzian-shaped Brillouin gain spectrum] is proportional to the acoustic attenuation and is given by the following relationship: $\frac{\Gamma_B}{2\pi}$. The acoustic attenuation is a function of several thermodynamic quantities and is given by²¹

$$\Gamma_B = \frac{q_B^2}{\rho} \left(\frac{(\gamma_h - 1)\kappa_C}{c_P} + \eta_b + \frac{4}{3}\eta_s \right), \quad (3)$$

where γ_h is the heat capacity ratio, κ_C is the thermal conductivity, c_P is the specific heat capacity at constant pressure, and η_b and η_s are the volume (bulk) and shear viscosities, respectively. Addressing more specifically the case under study of a gaseous medium, it is apparent from Eq. (3) that the acoustic attenuation of a sound wave in gas is mainly caused by the thermal conductivity and the viscous forces simply arising from the random motion of the gas molecules.

Thermal conduction is defined as energy diffusion across a temperature gradient (from higher to lower temperatures). The shear viscosity, however, is the result of a momentum transfer due to thermal diffusion which, in the presence of a velocity gradient, leads the gas molecules to diffuse from the higher to the lower flow velocity. The strength of the two processes highly depends on the strength of the gradients. The bulk viscosity involves the slow, irreversible energy exchange between the internal degrees of freedom (e.g., rotational and vibrational modes) and the translational mode. This transfer of energy has an opposing direction at each π -phase shift of the wave and leads to attenuation of the acoustic wave.²²

We can see from the expression of the electrostrictive coefficient $\gamma_e = \rho \frac{\partial \epsilon_r}{\partial \rho}$ that it is directly proportional to the gas density, and from Eq. (3), it is apparent that the acoustic attenuation is inversely proportional to the gas density. Accordingly, and given that in ideal gas conditions, the gas density is proportional to the gas pressure, we can understand from Eq. (2) that the Brillouin gain shows a square dependence on the gas pressure. This remarkable observation has already been presented in Ref. 12, where it has also been demonstrated experimentally using a gas-filled bandgap photonic crystal fiber. In our work, we make use of this square dependence of the Brillouin gain on the gas pressure and present it experimentally for the first time in gas-filled anti-resonant hollow-core optical fibers, as will be shown later in the paper in Sec. III. The scanning electron microscope (SEM) images of the fibers utilized in the experiments are shown in Figs. 1(a)–1(c), where D stands for the fiber core diameter.

C. Acousto-optic overlap effective area

To be able to estimate the acousto-optic overlap effective area A_{ao} present in Eq. (2), we simulated and studied the optical and acoustic modes in our gas-filled hollow-core fibers by means of a finite element method simulation using the COMSOL Multiphysics software, more specifically the two-dimensional “Electromagnetic waves” and “Pressure acoustics” modules. The silica refractive index $n_{\text{silica}} = 1.44$ and the gas refractive index $n_{\text{N}_2} = 1.000\,2697$ at atmospheric pressure and $n_{\text{N}_2} = 1.009\,3304$ for 35 bars of N_2 were entered into the calculation of the optical modes. The effective refractive index of the fundamental optical mode n_{eff} was calculated to be $0.990\,6697$ at atmospheric pressure and $0.999\,7304$ for 35 bars of

N_2 at a wavelength of $1.55\,\mu\text{m}$. As can be clearly noticed, the effective refractive index is smaller than unity, and this is a characteristic of hollow-core fibers given that the core, where most of the light is propagating, has a refractive index that is lower than the surrounding material (the cladding).²³ This is different from the effective refractive indices of conventional silica fibers that are greater than 1, given that, in this case, the core of the fiber has a refractive index that is greater than the cladding. Note that this is the index related to phase velocity and does not break the relativistic rule related to information velocity. At 35 bars of N_2 , the gas density $\rho_{\text{N}_2} = 29.6\,\text{kg/m}^3$ (using the ideal gas approximation) and the acoustic velocity $v_a = 358.5\,\text{m/s}$ (as deduced from the Brillouin frequency shift of our measurement) were used to calculate the acoustic mode in the fiber core, considering a sound hard boundary on the hollow tube wall. The acoustic mode profile of the excited modes was calculated for a wavenumber $\beta_{\text{ac}} = 8.107 \times 10^6\,\text{rad/m}$ ($\beta_{\text{ac}} = 2 \times \beta_{\text{op}}$ with $\beta_{\text{op}} = \frac{2\pi n_{\text{eff}}}{\lambda}$ as the propagation constant of the optical mode¹⁹) at a resonant frequency of 465 MHz, which corresponds to the measured Brillouin frequency shift at 35 bars of N_2 gas. For the analysis of the acoustic modes, we assume that the silica walls are rigid for the acoustic wave under consideration. With this simulation, we can compute the acousto-optic effective area A_{ao} , indicating the excitation strength of the acoustic mode under consideration, as given by²⁴

$$A_{ao} = \left(\frac{\int I_{\text{opt}} dA}{\int P \cdot I_{\text{opt}} dA} \right)^2 \cdot \int P^2 dA, \quad (4)$$

where I_{opt} is the intensity profile of the optical mode under consideration, P is the pressure profile of the dominant acoustic mode considered in the simulation, and $\int \dots dA$ designates the two-dimensional integral over the whole fiber cross-section. The fundamental optical and acoustic modes for the fibers used are illustrated in Fig. 1, where (d) is for the HC-PCF, (e) is for the HC-RAF, and (f) is for the HC-CAF. The calculated A_{ao} values are the following: $80\,\mu\text{m}^2$ for the PCF, $340\,\mu\text{m}^2$ for the CAF, and $905\,\mu\text{m}^2$ for the RAF (note that the order of the fibers is written from the lowest to the highest A_{ao}). Since A_{ao} is a function of fiber core area, it is understandable that the PCF shows the lowest value of the A_{ao} , followed by the CAF and then the RAF.

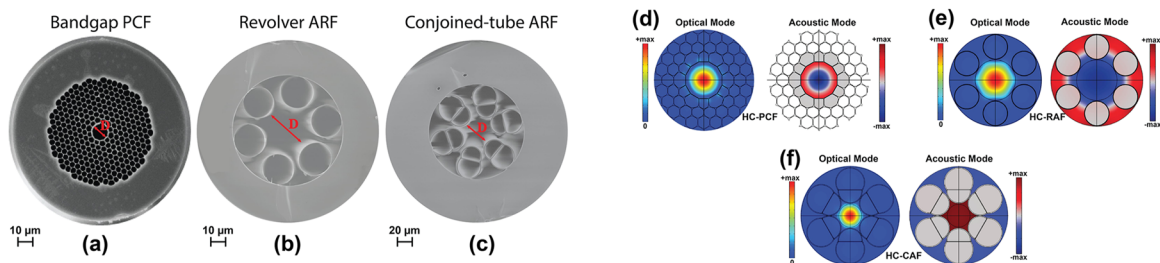


FIG. 1. Hollow-core optical fibers utilized in the experiments with D as the core diameter: (a) HC-PCF; (b) HC-RAF; and (c) HC-CAF. Graph showing the fundamental optical mode along with the fundamental acoustic mode for the fibers utilized in the experiments. The acoustic modes illustrated represent the dominant acoustic mode with the highest acousto-optic overlap. (d) HC-PCF; (e) HC-RAF; and (f) HC-CAF. Note: The circle in the center of the anti-resonant fibers does not indicate any boundary and is only used for visualization purposes. The figure is not to scale.

III. BRILLOUIN GAIN MEASUREMENT

A. Gas cell preparation

Light and gas coupling into the HCFs was achieved using a gas cell made of stainless-steel tubes that are connected to each other, three valves, two gas inlets/outlets, and one pressure meter, as can be seen in Fig. 2(a). Each cleaved end of the HCFs was butt-coupled to an angle-cleaved standard single-mode fiber patch cord using a coupling joint, which is made of two ceramic ferrules inside a sleeve with a side slit. The angle-cleaved fiber and the HCFs were aligned while leaving a few micrometers of spacing in between to enable gas flow into and outside of the HCFs. The total insertion loss due to the coupling was measured to be between about 8 and 12 dB, and a maximum reflection of ~ -55 dB was obtained. It ought to be remarked that we did not have the objective of optimizing the coupling loss, as the measured loss was low enough to conduct our experiments with no problems. A lower coupling loss can indeed be achieved, as has been shown in several works in the literature.^{25,26} The two coupling joints are carefully placed inside the stainless steel tubes, and the four fiber end sections are epoxy-glued. This configuration helps controlling the gas flow within the cell and achieving high purity of the gas by performing several rounds of vacuuming and purging before reaching the steady-state condition of the gas.

One important parameter to be taken into consideration while filling the cell with gas is the filling time. When the density is sufficiently large (e.g., density at atmospheric pressure), the gas flow in an HCF is in the hydrodynamic regime, and the flow can be approximated by the Poiseuille flow of an ideal gas.²⁷ For a sudden applied pressure P at the two fiber ends and a negligible initial pressure, which is much smaller than P , the filling time t_f is given by²⁸

$$t_f = \frac{32\eta_s L^2}{PD^2}, \quad (5)$$

where L is the fiber length. Using this equation, the approximate filling time of N_2 gas with $\eta_s = 18 \times 10^{-6}$ Pa s inside the cores of different HCF can be calculated. As apparent from Eq. (5), an increase in the shear viscosity results in a longer filling time. This means that for other gases that have lower shear viscosities (e.g., CO_2 has a $1.2\times$ lower shear viscosity than N_2 ($\eta_s = 15 \times 10^{-6}$ Pa s)), the filling time will be $1.2\times$ faster. Furthermore, t_f is directly dependent on L^2 and inversely proportional to D^2 and the pressure P . Given that

t_f is inversely dependent on D^2 —in the case when all other parameters in the equation are kept the same—we can expect that the PCF will require the longest gas filling times followed by the CAF then the RAF.

B. Experimental demonstration

1. Main experimental setup

The experimental setup opted for in the measurements of the Brillouin gain spectra relies on the heterodyne detection technique. Figure 2(b) shows the experimental setup where the laser used is a Toptica CTL1550 external-cavity diode laser (ECDL) with a 10 kHz linewidth. This narrow linewidth is necessary to be able to measure the Brillouin linewidth at high pressures, as will be seen in Sec. IV later on. The light is then guided into two branches using a 90/10 coupler. 10% of the laser light is amplified by an Erbium-doped fiber amplifier (EDFA), which is followed by a polarization controller (PC). The light hereafter passes from port 1 of the circulator through port 2 into the HCF under test. The average power measured at the input of the HCF is about 33 dBm. The HCF is filled with gas at different pressures. The back-reflected light is then transmitted from port 2 to port 3 and reaches a balanced-detection photo-detector (PD). 90% of the light from the coupler that is guided through the second branch (local oscillator) passes through an acousto-optic modulator (AOM) used as a frequency shifter, which is connected to a radio frequency (RF) generator whose frequency is set to 110 MHz. Accordingly, the frequency of the local oscillator is shifted by 110 MHz from the initial center frequency. The light then passes through another polarization controller and arrives at the PD. The average power measured at the PD is about -2 dBm. Heterodyne beating between the two branches occurs at the PD, and the Brillouin gain spectrum (BGS) for the whole fiber is acquired by an electrical spectrum analyzer (ESA). The experimental demonstration is conducted using one hollow-core bandgap photonic-crystal fiber (HC-PCF) and two anti-resonant fibers (ARFs), which are the hollow-core conjoined-tube ARF and the revolver ARF.

2. Estimation of the Brillouin gain experimentally

To be able to obtain the Brillouin gain experimentally, we need to calculate the back-reflected power coefficient R_B due to Brillouin

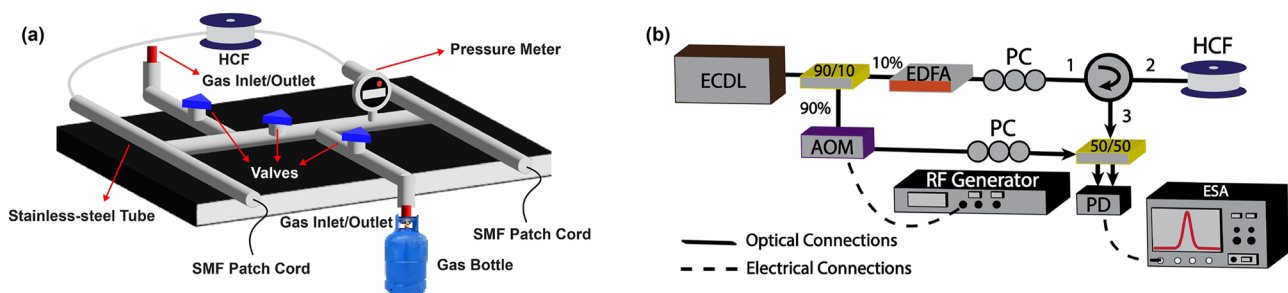


FIG. 2. (a) Graphic showing the final look of the gas cell assembly; and (e) experimental setup for the measurement of the Brillouin gain spectrum (BGS) (ECDL: External-cavity diode laser, EDFA: Erbium-doped fiber amplifier, PC: Polarization controller, AOM: Acousto-optic modulator).

back-scattering (considering the Stokes process), which is given by^{29,30}

$$R_B = Y_B e^{G_B/2} (I_0(G_B/2) - I_1(G_B/2)), \quad (6)$$

where I_m are the modified Bessel functions of the first kind of m -th order. The linear gain G_B is described as follows:

$$G_B = g_B P_P L, \quad (7)$$

with P_P as the input pump power and L as the length of the waveguide under test. The parameter Y_B in Eq. (6) is written as

$$Y_B = \frac{\pi}{2} (\bar{n} + 1) g_B h \nu_P \Delta \nu_B L, \quad (8)$$

where h is the Planck's constant, ν_P is the frequency of the input pump light, and $\Gamma_B = 2\pi\Delta\nu_B$ is the acoustic damping rate. The mean number of phonons \bar{n} per acoustic mode (with a frequency ν_B) at a temperature T is given by the Bose–Einstein distribution,

$$\bar{n} = \left(e^{\frac{h\nu_B}{k_B T}} - 1 \right)^{-1}, \quad (9)$$

where k_B is the Boltzmann constant. Since we are dealing with small gains $G_B \ll 1$, which is the case when the reflected light originates entirely from the scattering of the laser field by spontaneously (i.e., thermally) generated phonons, we can approximate the reflection coefficient to $R_B \approx Y_B$ and the reflected power to

$$P_{\text{SpBs}} = R_B P_P \approx Y_B P_P = \frac{\pi}{2} (\bar{n} + 1) h \nu_P \Delta \nu_B G_B. \quad (10)$$

Using Eq. (10) and rearranging while considering the possible losses (coupling and path losses), we finally yield the Brillouin gain measured experimentally. The value of P_{SpBs} , however, needs to be calibrated, as will be shown in the following sections.

3. Back-reflected power calibration

When two signals are coupled by a 50/50 coupler to beat at a balanced detector, the electrical amplitude V measured is

$$V \propto \sqrt{P_1 P_2}, \quad (11)$$

where P_1 and P_2 are the optical powers of the two signals beating at the photo-detector. Accordingly, the electrical power is equal to

$$P_E \propto V^2 \propto P_1 P_2 \Rightarrow P_E = \alpha_c P_1 P_2, \quad (12)$$

where α_c is a conversion coefficient, which should be fixed given that the same photo-detector and the same ESA are used. All the settings chosen in the ESA (e.g., RBW, VBW, scan range, attenuation, sampling points, etc.) should remain the same. From the power spectrum measured by the ESA, we can calculate the overall electrical power P_E by integrating over the frequency range, which is written in the form of a discrete summation as given by the following expression:

$$P_E = \sum P_{E,i} \Delta f = \Delta f \sum P_{E,i}, \quad (13)$$

where $P_{E,i}$ and Δf are the observed electrical power at each sampling point in the spectrum and the frequency step between two sampling points, respectively. Hence, α_c can be calculated with a calibration process (see Sec. III B 4), using a beating signal whose beating frequency is the same as the Brillouin scattering, and the optical powers of the two optical signals P_1 and P_2 are known. By substituting Eq. (12) into Eq. (13) and solving for α_c , we yield the following expression:

$$\alpha_c = \frac{\Delta f \sum P_{E,i}^{\text{calib}}}{P_1 P_2}. \quad (14)$$

Once α_c is obtained, the power of the back-reflected Brillouin signal can be calculated using the optical power of the local oscillator P_{LO} and the measured electrical power spectrum $P_{E,i}^{\text{SpBs}}$ as follows:

$$P_{\text{SpBs}} = \frac{P_1 P_2 \sum P_{E,i}^{\text{SpBs}}}{P_{LO} \sum P_{E,i}^{\text{calib}}}. \quad (15)$$

The value of P_{SpBs} is then substituted into Eq. (10) to calculate the linear gain G , from which the experimental Brillouin gain coefficient g_B is obtained.

4. Calibration setup

The Stokes and anti-Stokes powers are calibrated by using the calibration setup depicted in Fig. 3(a). A distributed feedback (DFB)

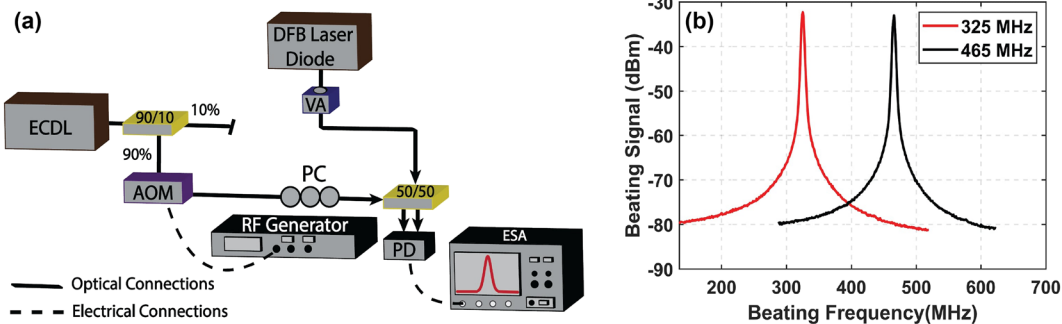


FIG. 3. (a) Calibration setup; (b) calibration spectra for the two different BFS of CO₂ (around 325 MHz) and N₂ (around 465 MHz).

laser diode is used, whose signal beats with the signal that is coming from the second branch of the Brillouin gain measurement setup [Fig. 2(b)], which has an ECDL as the laser source. The power from the DFB laser is adjusted by means of an attenuator such that the DFB laser power reaching the 50/50 coupler is about -10 dBm. The calibration is carried out by measuring the response of the photodetector at the frequencies of interest, and accordingly, we tune the frequency difference between the DFB laser and the ECDL to be in the region of the Stokes beating frequency (465 MHz for N_2 gas and 325 MHz for CO_2 gas). The beating spectra at these two frequency regions are shown in Fig. 3(b). The information about the powers from the calibration setup is used in Eq. (15) to calculate the power of the back-reflected Brillouin signal.

IV. EXPERIMENTAL AND THEORETICAL RESULTS

A. Results using nitrogen gas

Figure 4 from (a) to (d) shows the graphs of several obtained parameters as functions of the applied gas pressure for N_2 gas. As can be seen in Figs. 4(a) and 4(b), the Brillouin gain is increasing with respect to the increase in gas pressure. It should be noted that the square relationship between the Brillouin gain and the gas pressure mentioned in Sec. II can be inferred from the log-log graph that shows an increasing slope of about 2.07 ± 0.06 (HC-RAF), 2.05 ± 0.13 (HC-CAF), and 2.11 ± 0.08 (HC-PCF) in the case of N_2 and about 2.12 ± 0.12 (HC-RAF), 2.14 ± 0.14 (HC-CAF), and 2.06 ± 0.09 (HC-PCF) in the case of CO_2 , which indicates the square dependence. The circles in Fig. 4(b) represent the experimental values obtained during the measurement, and the solid lines correspond to the theoretical estimation of the gain using Eq. (2). From Eq. (2), it is apparent that the Brillouin gain is inversely proportional to the acousto-optic effective area of the fibers. A stronger acousto-optic interaction occurs when light and sound are confined

to a smaller area. Accordingly, depending on the core diameter, the gain will vary with respect to the different fibers if they have different core sizes as shown by the values provided in Table I. The graph includes the Brillouin gain of three types of hollow-core fibers, namely, HC-PCF, HC-CAF, and HC-RAF. The acousto-optic effective area has been calculated theoretically (as in Sec. II C) with the aid of the finite element method (FEM) using COMSOL Multiphysics software. Since the PCF has the smallest core diameter ($D = 10 \mu m$), the acousto-optic effective area is calculated to be $A_{ao} = 80 \mu m^2$ for N_2 gas. It can also be observed that the Brillouin gain provided by the HC-CAF is higher than that of the HC-RAF. This $\sim 2.75\times$ higher gain is directly attributed to the $\sim 2.66\times$ smaller acousto-optic effective area A_{ao} of the HC-CAF ($A_{ao} = 340 \mu m^2$) in comparison with that of the HC-RAF, which is about $A_{ao} = 905 \mu m^2$. It ought to be remarked that the slight difference in the ratios may be attributed to experimental errors. The graphs in Figs. 4(c) and 4(d) show the Brillouin frequency shift and the Brillouin linewidth as a function of the gas pressure, respectively.

B. Results using carbon dioxide gas

The results for the CO_2 gas are shown in Fig. 4 from (e) to (h). It can be observed from Fig. 4(e) that the gains for the different fibers are larger for CO_2 when compared to N_2 . This larger gain is a result of its more massive molecular structure in comparison with N_2 . Heavier gases like CO_2 and SF_6 were shown to exhibit higher Brillouin gains,¹² which are caused by the medium being denser as a result of the molecules occupying a larger volume in the medium. Their massiveness, however, comes with a rather significant drawback, namely, inevitable absorption lines in the infrared spectral region due to their more complex molecular structure, which enables a wide range of rotational-vibrational transitions. This problem is not encountered when lighter gases like N_2

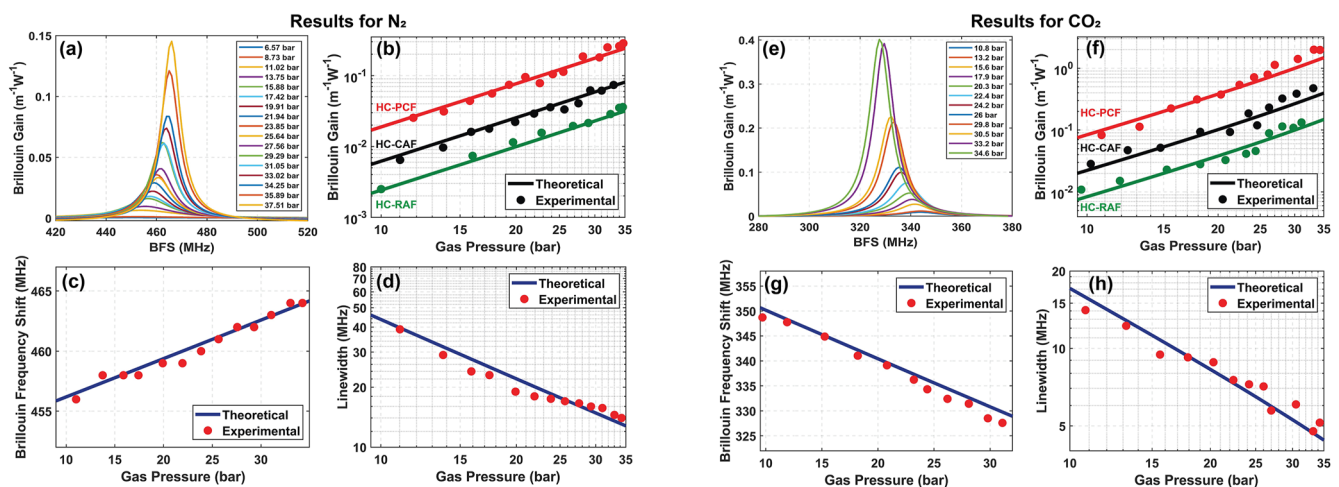


FIG. 4. Experimental results for N_2 and CO_2 gases: (a) and (e) Brillouin gain spectra of the HC-CAF with respect to pressure changes with the Brillouin gain coefficient on the y axis and the Brillouin frequency shift on the x axis; (b) and (f) Brillouin gain as a function of the gas pressure; (c) and (g) Brillouin frequency shift vs the gas pressure; and (d) and (h) Brillouin linewidth vs the gas pressure. Note that figures (a) and (e) were smoothed by a moving average filter to clarify the trend of the curves. In addition, note that the values in (c), (d), (g), and (h) are mostly the same irrespective of the fiber used, as these quantities are purely dependent on the gas's physical properties and not the fiber itself.

TABLE I. Acousto-optic effective area and Brillouin gain values obtained for the three different types of fibers used in the experiments for a pressure of 34.7 bars. The fibers used have the following core diameters: $D = 10\ \mu\text{m}$ for the bandgap PCF, $D = 22\ \mu\text{m}$ for the conjoined-tube ARF (CAF), and $D = 35\ \mu\text{m}$ for the revolver ARF (RAF). The typical Brillouin gain for a standard single-mode fiber (SMF) with $D = 8\ \mu\text{m}$ is about $0.28\ \text{m}^{-1}\ \text{W}^{-1}$.

Parameter	Fiber type		
	PCF	CAF	RAF
Acousto-optic area (μm^2)	80	340	905
Brillouin gain ($\text{m}^{-1}\ \text{W}^{-1}$)	0.285	N ₂ gas	0.029
		CO ₂ gas	
Brillouin gain ($\text{m}^{-1}\ \text{W}^{-1}$)	1.44	0.383	0.145

are used. Figure 4(g) shows the Brillouin frequency shift in the case of CO₂ gas, and we can see that it is around 100 MHz smaller than that of N₂ gas. The Brillouin linewidth shown in Fig. 4(h) for CO₂ gas is about $3\times$ narrower than that of N₂ gas. This difference can be explained by the different thermodynamic quantities corresponding to each of the gases.

C. Comparing the BFS results

Since the acoustic velocity plays a crucial role in the determination of the Brillouin gain, linewidth, and frequency shift, we would like to shed some light on it and understand how it varies with respect to the medium in which the sound is propagating. Unlike light, which is a transverse wave that can propagate without having any medium, a sound wave needs a medium to travel in and moves with a series of compressions and rarefactions. When it comes to sound waves, there is essentially no real particle movement; particles simply vibrate to and fro around their mean position, passing the sound energy from particle to particle while oscillating. Sound is a mechanical wave that depends on the elasticity of the medium as well as its density.

In solids, since the distance between molecules is very small (solids and liquids exhibit stronger cohesion forces between molecules compared to gases), any momentum transfer is much faster leading to significantly higher speeds of sound in solid media. Besides, solids and liquids are more rigid (i.e., less compressible) than gases, and this higher stiffness results in larger sound speeds in solid and liquid media as compared to gaseous ones. For a standard silica fiber at a wavelength of $1.55\ \mu\text{m}$, for example, the speed of sound is around 5972 m/s. This value is about an order of magnitude higher than the speed of sound in gases. It should be noted that under ideal gas conditions, the acoustic velocity is independent of the medium's pressure and density and is directly proportional to temperature changes. However, under non-ideal gas conditions, the changes in pressure and density can no longer be neglected and have to be taken into consideration. Accordingly, the ideal gas law is modified using corrections such as the virial coefficients to adequately represent the non-ideal gas conditions.

In our experiments, we are dealing with non-ideal gas conditions, and the speed of sound values for each pressure can be directly inferred experimentally from the Brillouin frequency shift

(BFS) values [Fig. 4(c) for N₂ gas and Fig. 4(g) for CO₂ gas] using the expression in Eq. (1). From these two figures, we can observe that the BFS of N₂ is about 100 MHz larger than that of CO₂. This can be explained by the fact that lighter molecules move faster (at a given constant temperature), and since the speed of sound (v_a) in gases is proportional to the speed (on average) of the molecules (v_{rms}), using the following expression: $v_a = \sqrt{\frac{\gamma_h}{3}} v_{\text{rms}}$ with γ_h as the specific heat ratio, the sound accordingly travels faster. Therefore, the sound speeds inside a medium filled with lighter molecules become higher, and thus the BFS is also larger, whereas the BFS is lower in media filled with more massive molecules, such as those of a CO₂ gas.

We also see from these same figures [Fig. 4(c) for N₂ gas and Fig. 4(g) for CO₂ gas] that with respect to increased pressure, the BFS (the acoustic velocity as well) gets higher in the case of N₂ gas, but it decreases in the case of CO₂. This is again related to the different masses of the molecules.

The greater the inertia (i.e., mass density) of individual particles in the medium, the less responsive they will be to intermolecular interactions, and this will make the speed of sound slower. To elaborate, it should be mentioned that the sound speed is slowed down in more dense media. This, however, might raise the question of why the speed of sound is faster in solids and liquids despite them being denser media. The reasoning in this case is not linked to the density of the medium, but this phenomenon—as we mentioned earlier—is directly attributed to the fact that solids and liquids are significantly stiffer/more rigid than gases due to the strong intermolecular cohesive forces and are nearly incompressible. Therefore, when it comes to a comparison between the different states of matter, the elastic properties of the medium have the largest impact on the behavior of the molecules and, therefore, on the sound speeds. As is widely known, sound waves are faster in solids than in liquids than in gases. However, when the comparison is made within the same phase of matter, the inertial property of density tends to be the property that has the greatest impact on the speed of sound. Accordingly, when comparing the speeds of sound in different gases, we will see that sound waves will travel faster in less dense media as opposed to more dense ones, which clearly explains the discrepancy in the trends between the N₂ and the CO₂ gases.

V. DISTRIBUTED TEMPERATURE MEASUREMENT

After having understood the behavior of the acoustic velocities in the different gaseous media, it becomes highly interesting to utilize the system and benefit from the high Brillouin gains in applications like distributed optical sensing. Brillouin-based distributed sensing systems using conventional solid-core silica fibers suffer from strain and temperature cross-sensitivity. In Ref. 12, it has been shown that the use of gas-filled hollow-core optical fibers can successfully eliminate this cross-sensitivity, and accordingly, highly-accurate strain-insensitive temperature measurements can be achieved. This is because the gaseous medium inside HCFs is not subject to shear stress in contrast with the conventional silica medium, which results in the sensor being insensitive to any strains applied in the surrounding environment. The experimental demonstration was carried out using a CO₂-filled HC-PCF. Here, we employ a gas-filled conjoined-tube anti-resonant hollow-core optical fiber as a proof-of-concept to demonstrate the capabilities of

emerging anti-resonant HCFs to be utilized for distributed temperature sensing while testing the response of different gases. This way, we benefit from the significantly lower loss that anti-resonant fibers can provide and accordingly take advantage of the real essence of distributed sensing, which is conducting measurements over longer distances.

A. Experimental setup

The demonstration of the temperature measurement is performed using Brillouin optical correlation-domain (also referred to as coherence-domain) reflectometry (BOCDR). The working principle of BOCDR is described in detail in Ref. 31. It is a technique that can reach high spatial resolutions and only requires single access to the fiber under test. As shown in Fig. 5(a), the light from the DFB laser is split into two branches by means of a 90/10 coupler, where 10% of the light is amplified by an Erbium-doped fiber amplifier (EDFA) followed by a polarization controller. A circulator is then used so that the light propagates from port 1 to port 2 into the fiber under test (21 m long) with a hotspot (2 m) positioned at the far end, gets backscattered, and passes through port 3, where it reaches a 50/50 coupler. The light in the 90% branch passes through a 1.6 km delay fiber, a polarization controller, and is combined with the spontaneous Brillouin backscattering using the 50/50 coupler to beat at a 1 GHz photo-detector (PD). The light is frequency dithered by tuning the current of the laser, and the heterodyne beating at the PD results in a correlation peak when the scattered light is in-phase with the reference light. When the two beating signals are

in phase, the BGS can be measured, whereas when they are out-of-phase, there will be no correlation peak and the BGS vanishes. Hence, the correlation peak may be randomly positioned on the fiber when the laser modulation frequency is swept. The BGS is then acquired by an electrical spectrum analyzer (ESA) for further analysis. Unlike in the experimental setup presented in Ref. 31, in our setup presented in Fig. 5(a), only one EDFA was required and no optical filtering was needed as a consequence of utilizing heterodyne detection during the experiment. Additionally, since the Brillouin frequency shift (BFS) is in the MHz range for the gas, no large bandwidth PD was necessary. The light source used is a distributed feedback laser with a linewidth measured to be around 3 MHz at a center frequency of 1550 nm, whose frequency is directly modulated using a sinusoid generated by a radio-frequency (RF) generator. There are two fundamental parameters that need to be characterized in a BOCDR system, namely, the measurement distance D_m and the spatial resolution R_{sp} , and they are governed by the following two expressions:

$$D_m = \frac{v_g}{2f_m}, \quad (16)$$

$$R_{sp} = \frac{v_g \Delta \nu_B}{2\pi f_m \Delta f}, \quad (17)$$

where v_g is the group velocity. We can see from Eqs. (16) and (17) that the measurement distance and the spatial resolution are functions of the modulation frequency and the modulation amplitude. The modulation frequency (f_m) is chosen to be 5.99 MHz, and the

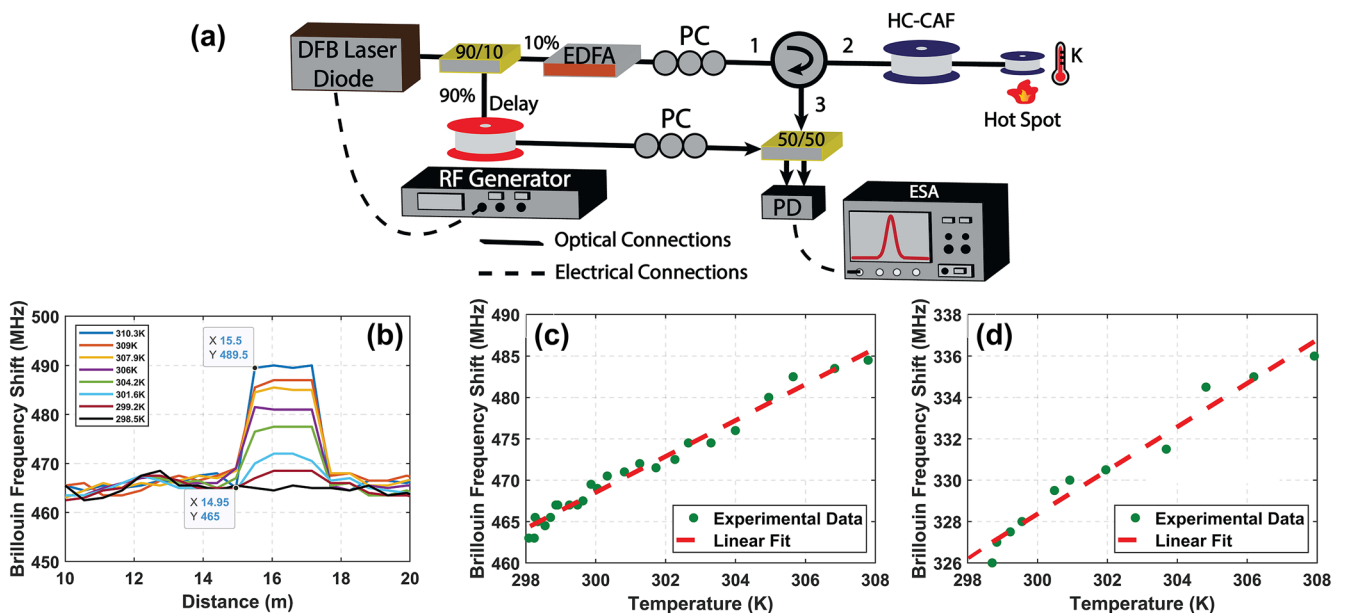


FIG. 5. (a) BOCDR experimental setup used for the temperature measurement: DFB: Distributed feedback laser, EDFA: Erbium-doped fiber amplifier, PC: Polarization controller, ESA: Electrical spectrum analyzer; (b) graph showing the Brillouin frequency shift at different temperatures as a function of distance; graphs showing the gas sensitivity (c) for nitrogen gas, which is about 2.18 ± 0.07 MHz/K; and (d) for carbon dioxide gas, which is about 1.05 ± 0.06 MHz/K.

modulation amplitude (Δf) is selected as 200 MHz, resulting in a spatial resolution of ~ 55 cm for a measurement distance that covered the full 21 m of our fiber under test. It should also be noted that the modulation amplitude is also limited by the BFS, and it has to be chosen in such a way that it is smaller than half of the BFS. This is because if it is larger than this proper value, the BGS might be buried inside reflections from the coupling end faces. Since the BFS in our case is around 465 MHz, a good enough margin would be around 200 MHz, which is our choice.

To make the correlation peak move along the fiber (21 m), the modulation frequency was tuned within a range of 35 kHz from 5.971 to 6.006 MHz. For the temperature measurement, we only tuned within a range of 16 kHz (corresponding to 10 m of the fiber) from 5.985 to 6.001 MHz, which is a range around the hotspot. At the hotspot, we placed ~ 2 m of the fiber on a hot plate, and a thermocouple was used to measure the temperature, which varied over a range of 12 K.

B. Temperature measurement results

The results of the temperature measurement are presented in Fig. 5(b). The longitudinal distribution of the Brillouin frequency shift over a distance of 10 m along the HC-CAF is illustrated for varying temperatures. From the figure, we can clearly see that the hotspot is about 2 m in length. The spatial resolution is indicated as the length between the two points marked on the graph, which is calculated at 55 cm. The graphs showing the sensitivities for the two gases are depicted in Figs. 5(c) and 5(d), where the BFS is shown as a function of the different temperatures. Already from this graph, we can infer the sensitivity and see that it is around 2.18 ± 0.07 MHz/K for N_2 gas as the scattering medium. The sensitivity was also measured for CO_2 at 1.05 ± 0.06 MHz/K.

The result obtained from the temperature measurement is quite interesting, as it shows in Figs. 5(c) and 5(d) that the temperature sensitivity of the two gases used in the experiments varied with respect to the gas species. The relationship between temperature and the acoustic velocity in an ideal gas is governed by the following equation:

$$v_a = \sqrt{\frac{\gamma_h RT}{M_m}}, \quad (18)$$

where γ_h is the heat capacity ratio, R is the universal ideal gas constant, T is the gas temperature, and M_m is the molar mass. As can be inferred from Eq. (18), lighter gases show higher acoustic velocities, which is a well-known result confirmed by our experiments where lighter gases show larger Brillouin shifts. More quantitatively, the ratio $\frac{v_a(CO_2)}{v_a(N_2)}$ is theoretically equal to ~ 0.77 , while it is experimentally equal to ~ 0.70 by simply taking the ratio of the Brillouin frequency shifts (proportional to the acoustic velocities), which is not massively different but still significant. Since the acoustic velocity is measured using hyper-sounds (hundreds of MHz frequency), friction may have a larger impact than at audio frequencies, and the importance of viscosity would be larger. The ratio at audio frequencies is 0.735, as given by the tables. From Eq. (18), it can be deduced that

$$\frac{\Delta v_B}{v_B} = \frac{\Delta v_a}{v_a} = \frac{1}{2} \frac{\Delta T}{T}, \quad \text{so that} \quad \frac{\Delta v_B}{\Delta T} = \frac{1}{2} \frac{v_B}{T}. \quad (19)$$

Therefore, the temperature sensitivity is proportional to the Brillouin frequency shift (and thus the acoustic velocity). From the experimental results, we calculated the ratio of acoustic velocities in N_2 and CO_2 gases to be ~ 1.43 , whereas the ratio in temperature dependence is around ~ 2 . This noticeable discrepancy is quite intriguing, and a clear reason behind it is not yet fully understood, except that CO_2 is quite close to a gas-liquid state transition and cannot, therefore, be properly considered as an ideal gas.

The spatial resolution and the temperature uncertainty were limited by the linewidth of the Brillouin gain spectrum. In the case of N_2 gas, however, there is no limitation in terms of how much pressure can be applied, and accordingly, the linewidth can be further reduced with the increase in pressure, as can the spatial resolution and the temperature uncertainty of the measurement. On the other hand, the pressure in CO_2 cannot be increased indefinitely and was kept well below the state at which CO_2 gas liquefies. The same applies to other lighter gases, like methane, for instance. Even though such gases exhibit lower Brillouin gains, they can potentially have fairly high temperature sensitivities compared to heavier gases, which exhibit larger Brillouin gains.

As we can clearly understand from these results, this platform is very agile and can be adapted to different types of gases. It can be applied to various applications, and depending on the type of study, the suitable gas, gas pressure, gas temperature, etc., can be chosen.

VI. CONCLUSION

In this work, we experimentally demonstrated light-sound interaction in three different types of gas-filled hollow-core optical fibers, namely, a bandgap hollow-core photonic crystal fiber and two anti-resonant hollow-core fibers. Optical amplification in gas-filled anti-resonant fibers is presented for the first time, to our knowledge, using different gas fillings and gas pressures. Using a conjoined-tube anti-resonant fiber filled with CO_2 at 35 bars, we showed a Brillouin gain ($0.383 \text{ m}^{-1} \text{ W}^{-1}$), which is higher than in standard silica fibers ($0.28 \text{ m}^{-1} \text{ W}^{-1}$) and significantly larger than the highest reported Raman gain at $1.55 \mu\text{m}$ ($0.084 \text{ m}^{-1} \text{ W}^{-1}$) in a gas-filled photonic crystal fiber. Despite the fact that the optical amplification obtained using the bandgap photonic crystal fiber is noticeably higher at 35 bars of CO_2 ($1.44 \text{ m}^{-1} \text{ W}^{-1}$), HC-PCFs have much narrower transmission windows, as these are controlled by the photonic bandgap guiding mechanism. This issue is, however, mitigated by using anti-resonant fibers with their wide transmission windows, which enable the amplification scheme to operate over a wide spectral range. In addition, we verified experimentally that the square dependence of the Brillouin gain on the gas pressure—which has been demonstrated in a gas-filled photonic crystal fiber¹²—remains as anticipated and fully valid in the case of gas-filled anti-resonant fibers and, in turn, if a high-gain amplification is required, it can be achieved by simply increasing the gas pressure.

Another interesting study conducted in this work is the realization of a highly-sensitive distributed temperature sensor using a conjoined-tube anti-resonant fiber based on a conventional Brillouin reflectometer with a sub-m spatial resolution of 0.55 m and a temperature sensitivity of 2.18 ± 0.07 MHz/K (using N_2 gas). We demonstrated experimentally that N_2 gas has around $2\times$ the tem-

perature sensitivity of CO₂ gas, indicating that lighter gases (such as CH₄) may show even higher temperature sensitivities. Other lighter gases like helium and hydrogen may also exhibit exceptionally high temperature sensitivities, but utilizing them may not be the most ideal solution, as such gases can easily permeate through the glass cladding of the fiber.^{32,33} The distributed temperature sensor offers the key advantage of being strain-insensitive because of the absence of shear stress in the gaseous medium of the anti-resonant hollow-core fibers, eliminating the cross-sensitivity between strain and temperature that exists in standard silica fiber sensors that are based on Rayleigh and Brillouin scattering processes. It is also immune to a very wide extent to high-energy radiation as the radiative damage on molecular bonds is significantly lower in gases when compared to standard silica fibers, and this quality can be very beneficial in spaceborne situations or inside nuclear reactors where conventional silica fibers may suffer from photodarkening.³⁴ Even though gas-filled HC-PCFs have shown great capabilities to be used for distributed temperature sensing,¹² their sensing range is fairly limited by their propagation loss, which cannot be reduced any further because of the restricting frozen-in surface capillary waves.¹⁸ That is why the use of anti-resonant fibers appears to be an attractive choice in this case, as in such fibers, the overlap of the optical field with the glass surfaces is significantly smaller (~0.01%) than in HC-PCFs (~0.1%–1%), which results in the surface scattering being largely reduced leading to the achievement of very low propagation loss. Accordingly, the sensing range can be largely extended to several tens of kilometers. For this part of the work, the conjoined-tube anti-resonant fiber was selected to benefit from two important factors: (1) showing a decent Brillouin gain and (2) taking a reasonable amount of time for gas filling. According to our studies, the bandgap photonic crystal fiber utilized in our work would require 5× more time to be filled with gas when compared to the conjoined-tube anti-resonant fiber if both have the same lengths and experience the same conditions.

This novel platform based on measuring spontaneous Brillouin scattering in gas-filled anti-resonant fibers has the potential to be integrated in a myriad of applications, such as the realization of high-gain amplifiers, highly-coherent Brillouin gas lasers,¹² microwave filters, tunable delay lines, as well as in distributed optical fiber sensing applications. Brillouin amplification in gases can also be achieved as a result of the interaction between the evanescent optical field in a nano-fiber and the surrounding gas medium, as has been shown in Ref. 13. Such promising results indicate that this platform can be extended to other fields where it is of interest to characterize different fluids and solvents. They can be filled inside hollow-core anti-resonant fibers or in the vicinity of nano-fibers, and their viscoelastic properties can be quantified using our platform which, with some changes, may also be potentially applied to applications in spectroscopy and microscopy.

ACKNOWLEDGMENTS

The authors acknowledge the support from the Swiss National Science Foundation under Grant Agreement Nos. 178895 and 159897. In addition, the authors would like to acknowledge Dr. Fan Yang and Dr. Flavien Gyger for the fruitful discussions and their insightful comments.

AUTHOR DECLARATIONS

Conflict of Interest

The authors have no conflicts to disclose.

Author Contributions

Malak Galal: Conceptualization (lead); Data curation (lead); Formal analysis (lead); Investigation (lead); Methodology (lead); Software (lead); Validation (lead); Visualization (lead); Writing – original draft (lead); Writing – review & editing (lead). **Li Zhang:** Conceptualization (supporting); Formal analysis (supporting); Investigation (supporting); Methodology (supporting); Validation (supporting); Visualization (supporting); Writing – original draft (supporting); Writing – review & editing (supporting). **Shoufei Gao:** Resources (lead). **Yingying Wang:** Resources (lead). **Luc Thévenaz:** Conceptualization (equal); Data curation (supporting); Formal analysis (supporting); Funding acquisition (lead); Investigation (supporting); Methodology (supporting); Project administration (lead); Supervision (lead); Validation (supporting); Visualization (supporting); Writing – original draft (supporting); Writing – review & editing (supporting).

DATA AVAILABILITY

The data that support the findings of this study are available from the corresponding author upon reasonable request.

REFERENCES

- H. Sakr, Y. Chen, G. T. Jasion, T. D. Bradley, J. R. Hayes, H. C. H. Mulvad, I. A. Davidson, E. Numkam Fokoua, and F. Poletti, "Hollow core optical fibres with comparable attenuation to silica fibres between 600 and 1100 nm," *Nat. Commun.* **11**, 6030 (2020).
- J. M. Dudley and J. R. Taylor, "Ten years of nonlinear optics in photonic crystal fibre," *Nat. Photonics* **3**, 85–90 (2009).
- D. G. Ouzounov, F. R. Ahmad, D. Müller, N. Venkataraman, M. T. Gallagher, M. G. Thomas, J. Silcox, K. W. Koch, and A. L. Gaeta, "Generation of megawatt optical solitons in hollow-core photonic band-gap fibers," *Science* **301**, 1702–1704 (2003).
- F. Benabid and P. J. Roberts, "Linear and nonlinear optical properties of hollow core photonic crystal fiber," *J. Mod. Opt.* **58**, 87–124 (2011).
- P. Russell, "Photonic crystal fibers," *Science* **299**, 358–362 (2003).
- M. A. Duguay, Y. Kokubun, T. L. Koch, and L. Pfeiffer, "Antiresonant reflecting optical waveguides in SiO₂-Si multilayer structures," *Appl. Phys. Lett.* **49**, 13–15 (1986).
- F. Poletti, "Nested antiresonant nodeless hollow core fiber," *Opt. Express* **22**, 23807–23828 (2014).
- W. Ding, Y.-Y. Wang, S.-F. Gao, M.-L. Wang, and P. Wang, "Recent progress in low-loss hollow-core anti-resonant fibers and their applications," *IEEE J. Sel. Top. Quantum Electron.* **26**, 4400312 (2019).
- V. Michaud-Belleau, E. N. Fokoua, T. Bradley, J. R. Hayes, Y. Chen, F. Poletti, D. J. Richardson, J. Genest, and R. Slavik, "0.174 dB/km hollow core double nested antiresonant nodeless fiber (DNANF)," in *Optical Fiber Communication Conference* (Optica, 2022), p. Th4C.7.
- F. Benabid, J. C. Knight, G. Antonopoulos, and P. S. J. Russell, "Stimulated Raman scattering in hydrogen-filled hollow-core photonic crystal fiber," *Science* **298**, 399–402 (2002).
- P. S. J. Russell, P. Hölzer, W. Chang, A. Abdolvand, and J. C. Travers, "Hollow-core photonic crystal fibres for gas-based nonlinear optics," *Nat. Photonics* **8**, 278–286 (2014).

- ¹²F. Yang, F. Gyger, and L. Thévenaz, "Intense Brillouin amplification in gas using hollow-core waveguides," *Nat. Photonics* **14**, 700–708 (2020).
- ¹³F. Yang, F. Gyger, A. Godet, J. Chrétien, L. Zhang, M. Pang, J.-C. Beugnot, and L. Thévenaz, "Large evanescently-induced Brillouin scattering at the surrounding of a nanofibre," *Nat. Commun.* **13**, 1432 (2022).
- ¹⁴R. Prevedel, A. Diz-Muñoz, G. Ruocco, and G. Antonacci, "Brillouin microscopy: An emerging tool for mechanobiology," *Nat. Methods* **16**, 969–977 (2019).
- ¹⁵G. Antonacci, T. Beck, A. Bilenca, J. Czarske, K. Elsayad, J. Guck, K. Kim, B. Krug, F. Palombo, R. Prevedel *et al.*, "Recent progress and current opinions in Brillouin microscopy for life science applications," *Biophys. Rev.* **12**, 615–624 (2020).
- ¹⁶Y. Zhao, Y. Qi, H. L. Ho, S. Gao, Y. Wang, and W. Jin, "Photoacoustic Brillouin spectroscopy of gas-filled anti-resonant hollow-core optical fibers," *Optica* **8**, 532–538 (2021).
- ¹⁷Z. Xu, T. Li, C. Sima, Y. Long, X. Zhang, Y. Ai, M. Hong, M. Chen, B. Deng, D. Lv *et al.*, "Mid-infrared hollow-core fiber based flexible longitudinal photoacoustic resonator for photoacoustic spectroscopy gas sensing," *Photonics* **9**, 895 (2022).
- ¹⁸P. J. Roberts, F. Couny, H. Sabert, B. J. Mangan, D. P. Williams, L. Farr, M. W. Mason, A. Tomlinson, T. A. Birks, J. C. Knight *et al.*, "Ultimate low loss of hollow-core photonic crystal fibres," *Opt. Express* **13**, 236–244 (2005).
- ¹⁹G. P. Agrawal, "Nonlinear fiber optics," *Nonlinear Science at the Dawn of the 21st Century* (Springer, 2000), pp. 195–211.
- ²⁰L. Thevenaz, *Advanced Fiber Optics: Concepts and Technology* (EPFL Press, 2011).
- ²¹Z. Gu and W. Ubachs, "Temperature-dependent bulk viscosity of nitrogen gas determined from spontaneous Rayleigh–Brillouin scattering," *Opt. Lett.* **38**, 1110–1112 (2013).
- ²²B. Sharma and R. Kumar, "Estimation of bulk viscosity of dilute gases using a nonequilibrium molecular dynamics approach," *Phys. Rev. E* **100**, 013309 (2019).
- ²³E. A. J. Marcatili and R. A. Schmeltzer, "Hollow metallic and dielectric waveguides for long distance optical transmission and lasers," *Bell Syst. Tech. J.* **43**, 1783–1809 (1964).
- ²⁴A. Kobyakov, M. Sauer, and D. Chowdhury, "Stimulated Brillouin scattering in optical fibers," *Adv. Opt. Photonics* **2**, 1–59 (2010).
- ²⁵C. Wang, R. Yu, B. Debord, F. Gérôme, F. Benabid, K. S. Chiang, and L. Xiao, "Ultralow-loss fusion splicing between negative curvature hollow-core fibers and conventional SMFs with a reverse-tapering method," *Opt. Express* **29**, 22470–22478 (2021).
- ²⁶X. Wei, B. Shi, D. J. Richardson, F. Poletti, and R. Slavík, "Distributed characterization of low-loss hollow core fibers using EDFA-assisted low-cost OTDR instrument," in *Optical Fiber Communication Conference* (Optica Publishing Group, 2023), p. W1C–4.
- ²⁷J. Henningsen and J. Hald, "Dynamics of gas flow in hollow core photonic bandgap fibers," *Appl. Opt.* **47**, 2790–2797 (2008).
- ²⁸R. Wynne and B. Barabadi, "Gas-filling dynamics of a hollow-core photonic bandgap fiber for nonvacuum conditions," *Appl. Opt.* **54**, 1751–1757 (2015).
- ²⁹R. W. Boyd, K. Rzaewski, and P. Narum, "Noise initiation of stimulated Brillouin scattering," *Phys. Rev. A* **42**, 5514–5521 (1990).
- ³⁰S. Le Floch and P. Cambon, "Theoretical evaluation of the Brillouin threshold and the steady-state Brillouin equations in standard single-mode optical fibers," *J. Opt. Soc. Am. A* **20**, 1132–1137 (2003).
- ³¹Y. Mizuno, W. Zou, Z. He, and K. Hotate, "Proposal of Brillouin optical correlation-domain reflectometry (BOCDR)," *Opt. Express* **16**, 12148–12153 (2008).
- ³²R. T. Tsugawa, I. Moen, P. E. Roberts, and P. C. Souers, "Permeation of helium and hydrogen from glass-microsphere laser targets," *J. Appl. Phys.* **47**, 1987–1993 (1976).
- ³³P. Hacıoğlu, D. Lee, G. V. Gibbs, and S. T. Oyama, "Activation energies for permeation of He and H₂ through silica membranes: An ab initio calculation study," *J. Membr. Sci.* **313**, 277–283 (2008).
- ³⁴D. S. Bykov, O. A. Schmidt, T. G. Euser, and P. S. J. Russell, "Flying particle sensors in hollow-core photonic crystal fibre," *Nat. Photonics* **9**, 461–465 (2015).